

PhotoElectroChemistry: Fitting Procedure

Milan Skocic^{a,*}

^a*Framatome Technical Center, 30 Bld de L'Industrie, Espace Magenta, 71205, Le Creusot, France*

Abstract

The weighting terms for the numerical fitting procedure were defined using the definition of the χ^2 distribution and a scaling factor for the covariance matrix in order to correctly estimate the confidence intervals of fitted parameters. Moreover, the confidence intervals were helpful for determining the number of semiconductive contributions. Experimental spectra were successfully tested with up to 12 contributions over 3 different potentials.

1. Introduction

In the course of the last 30 years, photoelectrochemical techniques have been shown to be useful tools for characterizing oxidation layers. Interdisciplinary theoretical underpinnings were built [5, 12, 20, 22, 23] such as the Gärtner-Butler model [4, 6] which has been proven to be a simple and robust model for the photocurrent generation. Technical progresses were achieved, allowing to study oxide layers at macroscopic, mesoscopic, and microscopic scales [1, 19], or in-situ in high temperature corrosion conditions [3, 17].

Up to now, for complex oxide scales formed of several p-type and n-type phases, the complete description of the photocurrent energy spectra could not be achieved, and only semi-quantitative and/or partial information could be obtained on the nature of the phases present in the oxide layers. Recently, a new approach was proposed by Petit et al. [15] to analyze the photocurrent spectra which was applied to oxidized duplex stainless steels [9] as well as Ni-based and Zr-based alloys oxidized in LWR conditions [17]. The numerical fitting procedure allowed to obtain high quality fits of the experimental data. Nonetheless, the estimation of the confidence intervals was not implemented.

This paper presents the additional work carried out in order to implement the estimation of the confidence intervals based on the fitting procedure developed by Petit et al. [15]. The latter was rewritten in Python which is an open source interpreted programming language. It is largely used in the scientific community [9–11, 14] and it comes with optimized libraries for numerical computations [8, 21] and a high quality 2D visualization library [7].

2. Fitting procedure

It should be reminded that the low photocurrents are extracted from the overall electrochemical current using

a modulation of the light illuminating the sample. The modulation is obtained with a mechanical chopper placed on the optical path. The reference signal of the modulation is connected to the external reference input of a lock-in amplifier, whereas the current output is connected to the signal input of the latter, allowing to measure both the modulus, $|I_{ph}|$, and the phase shift, θ of the so called as-measured photocurrent, I_{ph} . Then, the latter is converted, at each photon energy, in a more useful value, $I_{ph}^*(h\nu)$, proportional to the quantum yield of the photocurrent, by dividing $I_{ph}(h\nu)$ by $\Phi(h\nu)/\Phi_{max}$, where $\Phi(h\nu)$ is the photon flux arriving onto the sample, and Φ_{max} its maximum value.

As I_{ph}^* is measured under modulated light conditions and thus actually was a complex number, it was proposed that the real part $\Re I_{ph}^*$ and the imaginary part $\Im I_{ph}^*$ of the photocurrent I_{ph}^* should be considered simultaneously when analyzing and fitting the photocurrent energy spectra, rather than the modulus $|I_{ph}^*|$ only, as it was the case up to now. Therefore, the overall complex photocurrent, I_{ph}^* , was written as shown in eq. 1.

$$\begin{aligned} I_{ph}^* &= |I_{ph}^*| \cdot \cos \theta + i |I_{ph}^*| \cdot \sin \theta \\ I_{ph}^* &= \sum_i |I_{ph,i}^*| \cdot \cos \theta_i + \sum_i |I_{ph,i}^*| \cdot \sin \theta_i \end{aligned} \quad (1)$$

where $|I_{ph,i}^*|$ and θ_i represent the modulus and phase shift, respectively, of the photocurrent issued from the i^{th} semi-conducting constituent of the oxide layer. For thin semi-conducting films such as those usually investigated in most corrosion studies, the space charge regions are low compared to penetration depth of the light. $|I_{ph,i}^*|$ may thus be expected, at a given applied potential, to follow the simplified form of the Gärtner–Butler model, i.e. in fact to obey to the eq. 2.

$$(|I_{ph,i}^*| \cdot E)^{\frac{1}{n}} = K_i \cdot (E - E_{g,i}) \quad (2)$$

*Corresponding author

Email address: milan.skocic@framatome.com (Milan Skocic)

where $E_{g,i}$ and K_i represent the energy gap and a proportionality value, respectively. It should be emphasized that the as-defined $|I_{ph,i}^*|$ is proportional to, but not equal, to the quantum yield for the i th semiconducting constituent. n depends on the band to band transition type, $n = 1/2$ for an allowed direct transition, and $n = 2$ for an allowed indirect transition. To our knowledge, the case where $n = 1/2$ (direct transition) was rarely observed in the case of passive films or more or less disordered thin oxide films.

In addition, as the space charge regions are likely to extend over the whole thickness of each phase in the oxide layer, it is assumed that the recombination of the photo-generated electron—hole pairs, and thus the phase shifts, θ_i , will not depend on the photon energy. A given vector of m ($E_{g,i}, K_i, \theta_i$) triplets represents the supposed number of semiconducting phases contributing to the photocurrent. The scalar function, D , to be minimized is given in eq. 3 which represents a measurement of the distance between the experimental and calculated data.

$$(|I_{ph,i}^*| \cdot E)^{\frac{1}{n}} = K_i \cdot (E - E_{g,i}) \quad (3)$$

3. Estimation of the confidence intervals

The scalar function to be minimized defined in 3 used for fitting the photocurrent spectra ensures a fairly fast convergence towards the $3m$ parameters defining the semi-conductive contributions. However, the as-defined scalar function could not be used for estimating the confidence intervals. An alternative scalar function was defined to be computed with the optimal parameters in order to estimate the confidence intervals. The statistics of curve fitting shows that the confidence intervals can be estimated using the least-squares method which can be applied to nonlinear systems [2, 13].

The least-squares regression uses the proprieties of the χ^2 distribution. Consequently, of the experimental measurements of the photocurrent spectra are assumed to follow the normal distribution. Moreover, the least-squares method can be strictly applied only when the experimental variances are known for each energy value of the photocurrent spectrum. Nonetheless, the latter are not always known as it is the case for the photoelectrochemical characterizations. Consequently, modifications of the relationships defined for the ideal situation were necessary.

3.1. Ideal Situation

The equation 4 presents the scalar function χ^2 defined in the least-squares method when the experimental variances σ_{exp}^2 are known. The residuals, ϵ , weighted by the inverse of variances are given by the equation 5. χ^2 is therefore defined as the sum of the weighted residuals as illustrated by the equation 6

$$\chi^2 = \sum_{h\nu} \frac{|I_{ph,calc} - I_{ph,exp}|^2}{\sigma_{exp}^2} \quad (4)$$

$$\epsilon = \frac{|I_{ph,calc} - I_{ph,exp}|^2}{\sigma_{exp}} \quad (5)$$

$$\chi^2 = \sum_{h\nu} \epsilon^2 \quad (6)$$

$\nabla\chi^2$ approaches zero when the parameter values are approaching the optimum values. The covariance matrix of the fitted parameters, σ_p^2 , can be estimated with the Jacobian, J_ϵ , of the weighted residuals [2] and its expression is given by the equation 12. For nonlinear systems, as it is the case for the photocurrent, the equation 12 is a first-order approximation. In fact, the approximation is valid because the second-order terms are close to zero which avoids to compute the Hessian [16].

$$\sigma_p = (J_\epsilon^T \cdot J_\epsilon)^{-1} \quad (7)$$

The diagonal terms of the covariance matrix represent the variances of the parameters. The P% confidence interval of the parameters, $CI_{P\%}$ is obtained by multiplying the standard deviations with the student coefficient, $t_{dof,P}$, with dof being the degree of freedom corresponding to number of experimental points of the photocurrent, N , minus the number of parameter, $3m$. The probability $P\%$ was set to 95%. The confidence intervals of the parameters are given by the equation 8.

$$CI_P = \sqrt{\text{diag}(\sigma_p^2)} \cdot t_{dof,P} \quad (8)$$

$$dof = N - 3m$$

3.2. Real Situation

The confidence interval can be estimated even when the experimental variances, σ_{exp}^2 , are not known. However, it is necessary to modify the equations presented in section 3.1. The objective is to define a scalar function, S , which behaves like χ^2 with a constant scaling factor g . The scalar function, S , is defined using real and positive weighting terms, w , as shown in equation 6. Similarly to the Equation 6, the S function corresponds to the sum of the weighted residuals ϵ' .

$$S = \sum_{h\nu} \frac{|I_{ph,calc} - I_{ph,exp}|^2}{w^2} \quad (9)$$

The weighting terms are defined in order to isolate the scaling factor, g , and the experimental variances such as illustrated by the equation 10. Therefore, the weighting terms are considered proportional to the experimental variances.

$$w = g \cdot \frac{1}{\sigma_{exp}^2} \quad (10)$$

Combining equation 9 and equation 10, the scalar function S becomes proportional to χ^2 . Moreover, $\frac{\chi^2}{\nu}$ goes to unity when the optimum values of the parameters are reached. Consequently, the scaling factor g can be computed with the optimum value of S as shown by the equation 11.

$$\begin{aligned} S &= g \cdot \chi^2 \\ \frac{S}{\nu} &= g \cdot \frac{\chi^2}{\nu} \simeq 1 \end{aligned} \quad (11)$$

The covariance matrix, σ_p , can therefore be estimated with the scaling factor g and the Jacobian of the weighted residuals, $J_{\epsilon'}$ as illustrated by the equation 12. The confidence intervals are then computed using the Equation 8.

$$\begin{aligned} \sigma_p'^2 &= (J_{\epsilon'}^T \cdot J_{\epsilon'})^{-1} \\ \sigma_p &= g \cdot \sigma_p'^2 \end{aligned} \quad (12)$$

The choice of the weighted terms was made considering that the experimental variances are proportional to average noise of the photocurrent modulus in dark conditions, $\bar{\epsilon}_d$. It has been proposed that the variances are smaller when the quantum yield is greater. The latter is represented by the photocurrent corrected by the photon flux normalized to its maximum value, $I_{ph,N}$. The normalization ensures that the weighting terms have the same dimension as the inverse of the variances as shown in equation 13. S is therefore adimensional as it is the case for χ^2 . The Jacobian, $J_{\epsilon'}$ is numerically estimated by fixing the finite difference step to the squared root of the machine precision [13, 16].

$$\begin{aligned} \sigma_{exp}^2 &\propto \frac{\bar{\epsilon}_d}{|I_{ph,N}|} \\ w &= \frac{1}{\sigma_{exp}^2} = g \cdot \frac{|I_{ph,N}|^2}{\bar{\epsilon}_d^2} \end{aligned} \quad (13)$$

4. Application

4.1. Numerically generated energy photocurrent spectra

The weighted terms, as previously defined, represent the signal/noise ratio. In order to test the relevancy of the weighted terms, energy photocurrent spectra were recomputed (eq. 1) from parameter values obtained by Petit et al. [15] by fitting a fairly simple energy photocurrent spectrum having 3 semiconductive contributions. The values of the parameters are presented in 1.

An increasing noise was added to the computed values of I_{ph} . The noise was calculated using a normal centered distribution $N(0, \sigma)$ where σ was set to the minimal value of the calculated photocurrent et then amplified using an amplification factor f_a . The generated noise was added to real and imaginary parts of the photocurrent I_{ph} . The modules of the corrected photocurrent I_{ph}^* for different

	$10^5 K_i$ $A^{1/2} \cdot eV^{1/2}$	θ_i $^\circ$	$E_{g,i}$ eV
	4.6	7.0	1.91
	5.4	-33.0	2.44
	7.0	156.0	3.16

Table 1: Parameter values obtained by Petit et al. [15] (figure 1) by numerical fitting.

amplification factors are shown in figure 1 and the corresponding values of the fitted parameters are presented in table 3. The confidence intervals increased when the signal/noise ratio decreased as it was expected.

The estimation of the confidence intervals can also be helpful for determining the number of semiconductive contribution in an energy photocurrent spectrum. In fact, the determination of the number of semiconductive contributions is an iterative operation by adding contributions until the spectrum is correctly fitted. The estimation of the confidence intervals can be used as a break point of the iterative search when the intervals of two contributions are overlapping i.e. they are no more statistically discernable.

For the sake of illustration, the energy photocurrent of the figure 1a was fitted by considering 3, 4 and 5 semiconductive contributions for energies ranging from 1.8 eV to 4.0 eV. Table 4 shows the bandgap values and the associated confidence intervals obtained after numerical fitting.

The numerical fitting, by considering 4 contributions, showed that the contribution with a bandgap value of 1.91 eV was split into two contributions (1.9 eV and 2 eV). The second one featured a confidence interval in the same order of magnitude as the value itself i.e. the 4th contribution did not improve the fitting of the experimental data. The numerical fitting, by considering 5 contributions, showed that the same splitting of the contribution with a bandgap value of 1.91 eV. Moreover, the contribution with a bandgap value of 2.4 eV was split into two contributions (2.6 eV and 2.7 eV) whose confidence intervals were overlapping indicating that they were not statically discernable.

4.2. Experimental energy photocurrent spectra

The defined procedure for estimating the interval confidences was then applied to energy photocurrent spectra recorded at different potentials on a Ni-based alloy 600 thermally oxidized. The experimental data were provided by Petit et al. [15]. The experimental, as well as the fitted, modules of the corrected photocurrent $|I_{ph}^*|$ are illustrated in figure 3.

The photocurrent modulus in dark conditions, $\bar{\epsilon}_d$, was computed by taking the average of the photocurrent modulus for the five highest energies (6.19, 6.17, 6.14 and 6.08 eV) where the emission spectrum of a Xe lamp can be reasonably considered close to zero. The photocurrent modulus featured a strong decrease for energies lower than 3 eV when the potential decreased towards more cathodic

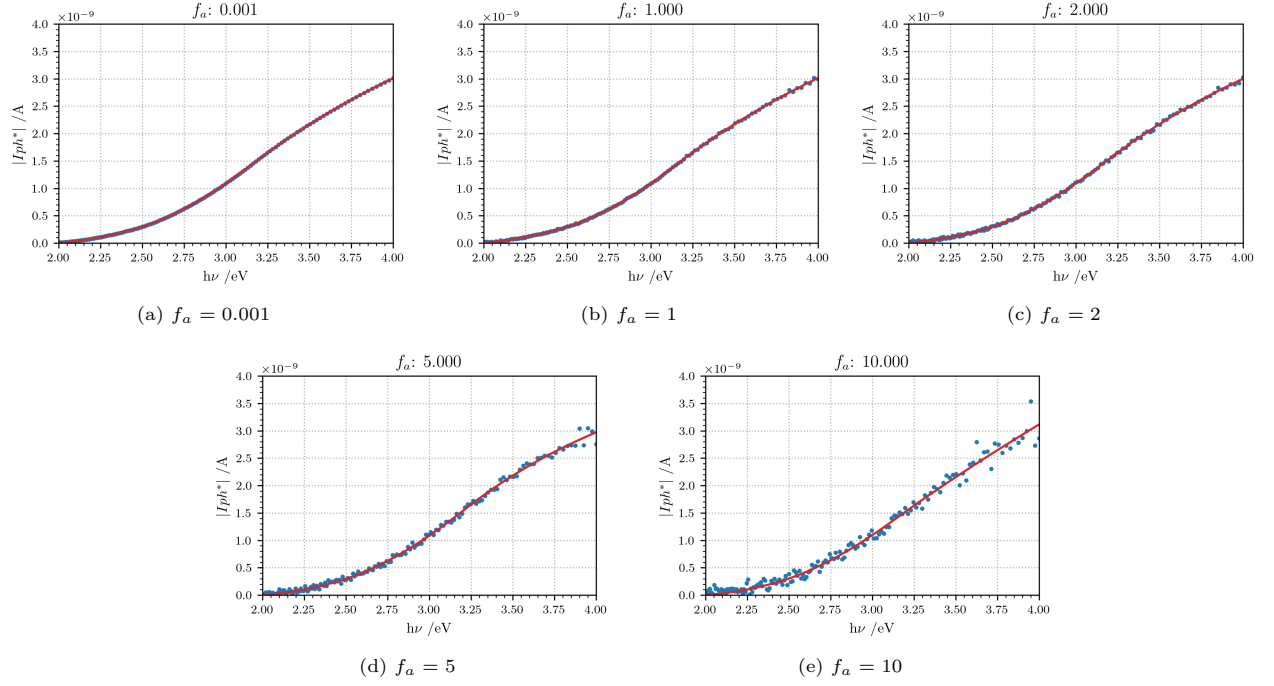


Figure 1: Energy photocurrent spectra generated with different amplification factors f_a .

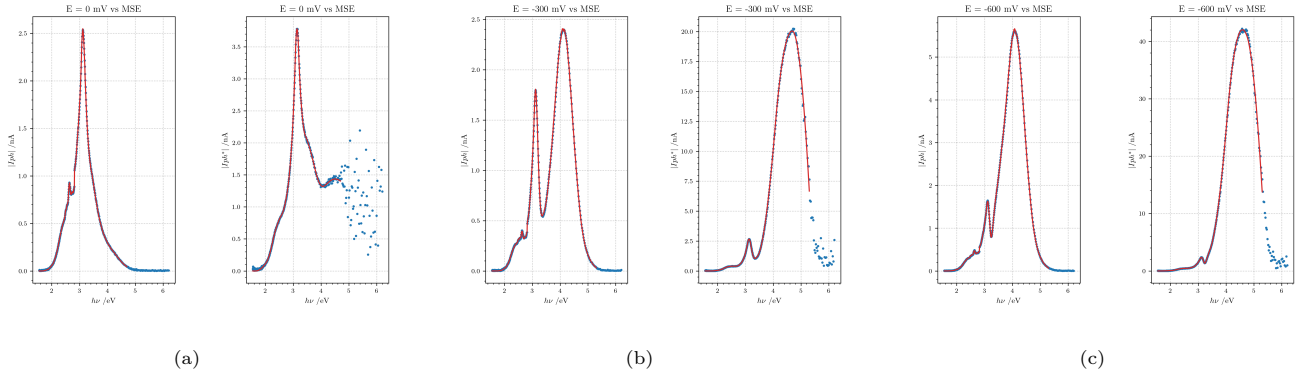


Figure 2: Energy photocurrent spectra recorded at different applied potentials on a Ni-based alloy A600 oxidized at 900°C in oxygen for 2h (according to [18]).

U mV	$10^5 K_i$ $A^{1/2}$ $eV^{1/2}$	θ_i $^\circ$	$E_{g,i}$ eV	$10^5 K_i$ $A^{1/2}$ $eV^{1/2}$	θ_i $^\circ$	$E_{g,i}$ eV	$10^5 K_i$ $A^{1/2}$ $eV^{1/2}$	θ_i $^\circ$	$E_{g,i}$ eV	$10^5 K_i$ $A^{1/2}$ $eV^{1/2}$	θ_i $^\circ$	$E_{g,i}$ eV
100	5.19 ± 0.09	-42.6 ± 0.5	1.74 ± 0.02	6.4 ± 0.4	122 ± 2	2.42 ± 0.04	6.5 ± 0.4	134 ± 4	2.88 ± 0.05	8.9 ± 0.8	-64 ± 6	3.47 ± 0.06
0	5.14 ± 0.07	-49.2 ± 0.5	1.755 ± 0.008	6.1 ± 0.3	120 ± 2	2.41 ± 0.04	6.8 ± 0.4	131 ± 4	2.82 ± 0.04	9.1 ± 0.9	-58 ± 6	3.48 ± 0.06
-100	4.7 ± 0.1	-52.4 ± 0.5	1.76 ± 0.02	6.1 ± 0.3	119 ± 2	2.44 ± 0.03	6.9 ± 0.4	131 ± 4	2.91 ± 0.04	9.2 ± 0.9	-56 ± 6	3.43 ± 0.06
-200	4.01 ± 0.06	-53.5 ± 0.6	1.76 ± 0.02	5.1 ± 0.4	121 ± 3	2.43 ± 0.04	6.1 ± 0.4	124 ± 4	2.85 ± 0.04	8.3 ± 0.7	-63 ± 6	3.46 ± 0.06
-300	2.9 ± 0.3	-52 ± 2	1.76 ± 0.05	4.2 ± 0.6	122 ± 5	2.42 ± 0.09	5.7 ± 0.5	122 ± 4	2.82 ± 0.08	7.6 ± 0.3	-64 ± 3	3.43 ± 0.06
-400	1 ± 2	-50 ± 30	1.7 ± 0.6	4 ± 3	120 ± 20	2.4 ± 0.5	5 ± 2	130 ± 20	2.8 ± 0.3	6.7 ± 0.7	-61 ± 6	3.35 ± 0.08

Table 2: Parameters values and the associated confidence intervals obtained after numerical fitting of the energy photocurrent spectra of the figure 3. The potential is referred with respect to mercury sulfate electrode (MSE, +650 V vs. SHE).

f_a	$10^5 K_i$ $A^{1/2} \cdot eV^{1/2}$	θ_i $^\circ$	$E_{g,i}$ eV
0.0001	4.6000 ± 0.0002 5.4000 ± 0.0004 7.0000 ± 0.0009	7.00 ± 0.02 -33.00 ± 0.02 156.00 ± 0.02	1.9100 ± 0.0002 2.4400 ± 0.0003 3.1600 ± 0.0009
1	4.6 ± 0.2 5.5 ± 0.4 7.0 ± 0.3	-7 ± 4 -33 ± 5 156 ± 4	1.91 ± 0.04 2.45 ± 0.08 3.15 ± 0.04
2	4.6 ± 0.6 5.5 ± 0.7 7.0 ± 0.5	-7 ± 7 -32 ± 20 160 ± 6	1.91 ± 0.09 2.4 ± 0.2 3.2 ± 0.2
5	5 ± 3 5 ± 3 7 ± 3	8 ± 30 -38 ± 50 154 ± 20	1.9 ± 0.4 2.4 ± 0.5 3.2 ± 0.2
10	5 ± 8 5 ± 6 6 ± 4	10 ± 80 -43 ± 200 -155 ± 60	1.9 ± 0.9 2 ± 2 3.1 ± 0.7

Table 3: Parameter values obtained by Petit et al. [15] (figure 1) by numerical fitting.

m	3	4	5
$E_{g,1}$	1.91 ± 0.07	1.9 ± 0.4	1.9 ± 0.1
$E_{g,2}$	2.4 ± 0.2	2 ± 5	2 ± 4
$E_{g,3}$	3.16 ± 0.06	2.5 ± 0.4	2.5 ± 0.2
$E_{g,4}$		3.16 ± 0.06	2.7 ± 0.2
$E_{g,5}$			3.2 ± 0.1

Table 4: Bandgap values and the associated confidence intervals obtained after numerical fitting of the energy photocurrent spectra of the figure 1a.

values indicating that the ratio signal/noise decreased as well.

Table 2 shows the parameters and the associated confidence intervals obtained after numerical fitting of the experimental data. The increase of the computed confidence intervals for the three first contributions, having bandgap values lower than 3 eV, mirrored correctly the decrease of the ratio signal/noise observed on the experimental data in figure 3.

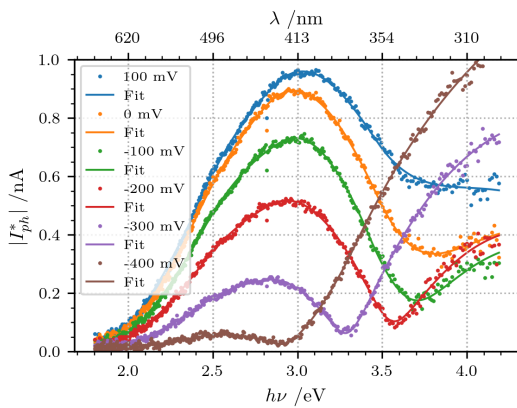


Figure 3: Energy photocurrent spectra recorded at different potentials on a Ni-based alloy 600 thermally oxidized (experimental data were provided by Petit et al. [15])

The fitting procedure was also applied to additional photocurrent spectra obtained by Srisrual [18] where up to 12 contributions were found to be statistically discernable

over 3 different potentials as illustrated in figure 2 and table 5.

	$0mV_{MSE}$	$-300mV_{MSE}$	$-600mV_{MSE}$
$E_{g,1}$	1.7 ± 0.2	2 ± 3	2 ± 20
$E_{g,2}$	2.0 ± 0.2	2 ± 3	2 ± 8
$E_{g,3}$	2.25 ± 0.09	2 ± 1	2 ± 4
$E_{g,4}$	2.58 ± 0.04	2.6 ± 0.3	3 ± 2
$E_{g,5}$	2.8 ± 0.04	2.9 ± 0.2	2.8 ± 0.9
$E_{g,6}$	2.96 ± 0.02	3.08 ± 0.01	3.09 ± 0.05
$E_{g,7}$	3.077 ± 0.0022	3.16 ± 0.03	3.2 ± 0.2
$E_{g,8}$	3.195 ± 0.003	3.19 ± 0.02	3.2 ± 0.05
$E_{g,9}$	3.27 ± 0.02	3.42 ± 0.03	3.42 ± 0.04
$E_{g,10}$	3.44 ± 0.03	4.073 ± 0.009	4.047 ± 0.008
$E_{g,11}$	3.8 ± 0.3	4.7 ± 0.1	4.7 ± 0.2
$E_{g,12}$	4.1 ± 0.5		

Table 5: Parameters values and the associated confidence intervals obtained after numerical fitting of the energy photocurrent spectra of the figure 2

4.3. Conclusion

The weighting terms for the numerical fitting procedure were defined using the definition of the χ^2 distribution and a scaling factor for the covariance matrix. The latter correctly reflected the noise of the experimental data in the computed i.e. the covariance matrix will correctly estimate the confidence intervals for the fitted parameters.

Moreover, the confidence intervals were helpful for determining the number of semiconductive contributions. The estimation of the confidence intervals can be used as a break point of the iterative search when the intervals of two contributions are overlapping i.e. they are no more statistically discernable.

Experimental spectra were tested with up to 12 contributions over 3 different potentials and the estimated confidence intervals were helpful at asserting that the semiconductive contributions are statistically discernable.

References

- [1] Benaboud, R., Bouvier, P., Petit, J.P., Wouters, Y., Galerie, A., 2007. Comparative study and imaging by PhotoElectroChemical techniques of oxide films thermally grown on zirconium and Zircaloy-4. *Journal of Nuclear Materials* 360, 151–158.
- [2] Bevington, P.R., Robinson, D.K., 2003. *Data Reduction and Error Analysis for Physical Sciences*. Third ed., McGraw Hill, New York.
- [3] Bojinov, M., Kinnunen, P., Laitinen, T., Mäkelä, K., Saario, T., Sirkiä, P., 2002. Photocurrent response of the passive film on iron in a high-temperature aqueous electrolyte. *Electrochemistry Communications* 4, 222–226.
- [4] Butler, M., 1977. Photoelectrolysis and physical properties of the semiconducting electrode WO_3 . *Journal of Applied Physics* 48, 1914. doi:10.1063/1.323948.

- [5] Di Quarto, F., Sunseri, C., Piazza, S., Sunseri, C., 1997. Semiempirical Correlation between Optical Band Gap Values of Oxides and the Difference of Electronegativity of the Elements. Its Importance for a Quantitative Use of Photocurrent Spectroscopy in Corrosion Studies. *Journal of Physical Chemistry* 101, 2519–2525.
- [6] Gärtner, W.W., 1959. Depletion-Layer Photoeffects in Semiconductors. *Physical Review* 116, 84–87.
- [7] Hunter, J.D., 2007. Matplotlib: A 2D graphics environment. *Computing In Science and Engineering* 9, 90–95.
- [8] Jones, E., Oliphant, T., Peterson, P., Others, 2020. SciPy: Open source scientific tools for Python. <http://www.scipy.org/>.
- [9] Kiusalaas, J., 2010. Numerical Methods in Engineering with Python. Second ed., Cambridge University Press, Cambridge.
- [10] Langtangen, H.P., 2012. A Primer on Scientific Programming with Python. Third ed., Springer, Berlin Heidelberg.
- [11] Millman, K.J., Aivazis, M., 2011. Python for Scientists and Engineers. *Computing in Science & Engineering* 13, 9–12. doi:10.1109/MCSE.2011.36.
- [12] Morrison, S.R., 1980. Electrochemistry at Semiconductor and Oxidized Metal Electrodes. Plenum Press, New York.
- [13] Nocedal, J., Wright, S.J., 2006. Numerical Optimization. Second ed., Springer, New York.
- [14] Oliphant, T.E., 2007. Python for Scientific Computing. *Computing in Science & Engineering* 9, 10–20. doi:10.1109/MCSE.2007.58.
- [15] Petit, J.P., Boichot, R., Loucif, A., Srisrual, A., Wouters, Y., 2013. Photoelectrochemistry of Oxidation Layers: A Novel Approach to Analyze Photocurrent Energy Spectra. *Oxidation of Metals* 1, 1–11.
- [16] Press, W.H., Teukolsky, S.A., Vetterling, W.T., Flannery, B.P., 2007. Numerical Recipes: The Art of Scientific Computing. Third ed., Cambridge University Press, Cambridge.
- [17] Skocic, M., 2016. Etude (photo)-électrochimique en réacteur simulé du phénomène de shadow corrosion des alliages de zirconium. Ph.D. thesis. Université de Grenoble Alpes. Grenoble.
- [18] Srisrual, A., 2013. Caractérisation Photoélectrochimique d'oxydes Thermiques Développés Sur Métaux et Alliages Modèles. Thèse de doctorat. Université de Grenoble.
- [19] Srisrual, A., Petit, J.P., Wouters, Y., Pascal, C., Galerie, A., 2011. Photoelectrochemical investigations on individual ferritic and austenitic grains of a duplex stainless steel oxidized in water vapour. *Materials at High Temperatures* 28, 349–354.
- [20] Stimming, U., 1986. Photoelectrochemical studies of passive films. *Electrochimica Acta* 31, 415–429.
- [21] Van der Walt, S., Colbert, S.C., Varoquaux, G., 2011. The NumPy Array: A Structure for Efficient Numerical Computation. *Computing in Science & Engineering* 13, 22–30. doi:10.1109/MCSE.2011.37.
- [22] Vijh, A.K., 1969. Correlation between bond energies and forbidden gaps of inorganic binary compounds. *Journal of Physics and Chemistry of Solids* 30, 1999–2005.
- [23] Wouters, Y., Galerie, A., Petit, J.P., 2007. Photoelectrochemical Study of Oxides Thermally Grown on Titanium in Oxygen or Water Vapor Atmospheres. *Journal of The Electrochemical Society* 154, C587–C592.